Environment International 201 (2025) 109548

Contents lists available at ScienceDirect

Environment International

journal homepage: www.elsevier.com/locate/envint

Full length article

Increased particle mass deposition on lung tissue due to industrial and waste-burning activities

Anusmita Das [a,b], Erwin W. Karg [c], George A. Ferron [c], Jürgen Schnelle-Kreis [a], Anil Kumar Mandariya [d], Gazala Habib [e], Alfred Wiedensohler [c], Mira L. Pöhlker [c], Ralf Zimmermann [a,b], Ajit Ahlawat [c,f,*]

[a] Joint Mass Spectrometry Center (JMSC) at Comprehensive Molecular Analytics (CMA), Helmholtz Zentrum München, Ingolstädter Landstrasse 1, D-85764 Neuherberg, Germany
[b] Joint Mass Spectrometry Center (JMSC) at Chair of Analytical Chemistry, Institute of Chemistry, University of Rostock, Albert-Einstein-Strasse 27, D-18059 Rostock, Germany
[c] Atmospheric Microphysics Department, Leibniz Institute for Tropospheric Research (TROPOS), 04318 Leipzig, Germany
[d] Univ Paris Est Créteil and Université Paris Cité, CNRS, LISA, F – 94010 Créteil, France
[e] Department of Civil Engineering, Indian Institute of Technology (IIT) Delhi, Delhi 110016, India
[f] Department of Geoscience and Remote Sensing, Delft University of Technology (TU Delft), 2628 CN Delft, the Netherlands

ARTICLE INFO

Handling Editor: Adrian Covaci

Keywords:
Atmospheric aerosol particles
Hygroscopicity
Density
Lung deposition
Tissue deposition dose

ABSTRACT

Understanding airborne particle mass deposition in the lungs is crucial for assessing health effects, particularly in regions with severe air pollution. While several studies have modelled lung deposition, there is limited information on lung tissue deposition that incorporates factors like hygroscopicity and density in polluted environments or source-specific exposures. This study examines the impact of atmospheric aerosol properties, including particle number size distribution, effective density, and hygroscopic growth, on lung tissue deposition using data from a measurement campaign in Delhi, India. Using the Hygroscopic Particle Lung Deposition (HPLD) model, the number (TD_n) and mass (TD_m) of tissue-deposited particles were calculated for various episodes: biomass burning (*BB*), chloride (*Cl*), hydrocarbon-like organic aerosol (*HOA*), and relatively clean (*RC*) periods. Chloride episodes, linked to industrial and waste burning activities, showed the highest tissue deposition mass (28 pg $cm^{-2}h^{-1}$), followed by *BB* (22 pg $cm^{-2}h^{-1}$), *HOA* (17 pg $cm^{-2}h^{-1}$), and *RC* (14 pg $cm^{-2}h^{-1}$) on total inner lung surface area. In addition, incorporating hygroscopicity and density increased deposition estimates by 1.8–2.8 times. This study underscores the importance of quantifying tissue deposition doses for improving exposure assessments, particularly in highly polluted regions where elevated particulate levels exacerbate lung inflammation, respiratory issues, and cancer risk.

1. Introduction

Air pollution contributes to 18 % of annual premature deaths in India (World Air Qual. Rep., 2019). Delhi, recognized as one of the most polluted cities in the world, experiences severe pollution episodes, especially during the post-monsoon and winter months, impacting climate, health, and economy (Lalchandani et al., 2022). Aerosol particles originating from various primary pollution sources (biomass burning, industry, vehicles, etc.) and secondary processes can penetrate deep into the respiratory tract (Oberdörster, 2000). To better understand the health impacts of atmospheric aerosols, it is necessary to integrate micro- and macroscopic particle properties. Previous research has demonstrated that molecular-level mechanisms significantly influence the initial growth of particles. Gas-phase interactions, adsorption behavior and chemical composition at the nanoscale shape particle evolution, ultimately affecting their physical characteristics. These factors influence the partitioning of precursors between phases, subsequently leading to the formation or modification of aerosol properties (Kaviani et al., 2022b; Kaviani et al., 2022a, Kaviani et al., 2019). Laboratory studies have shown that the chemical composition and acidity of newly formed nanoparticles strongly influence their hygroscopic properties, particularly during the nucleation-to-growth

---

* Corresponding author at: Department of Geoscience and Remote Sensing, Delft University of Technology (TU Delft), 2628 CN Delft, the Netherlands
E-mail address: a.s.ahlawat@tudelft.nl (A. Ahlawat).

https://doi.org/10.1016/j.envint.2025.109548
Received 23 January 2025; Received in revised form 15 May 2025; Accepted 21 May 2025

transition (Chee et al., 2019; Chen et al., 2018). These findings provide essential context for understanding how particles transition from freshly nucleated clusters to larger, respirable aerosols whose macroscopic properties govern deposition and health outcomes. The macroscopic factors that influence the particle deposition in the respiratory tract include the physical and chemical properties of aerosol particles (such as the size distribution, density, shape, surface area concentration, and hygroscopicity), the anatomy of the respiratory tract (diameter, length, and breathing angles of airway segments) and its physiology (including airflow and breathing patterns) (Morawska and Buonanno, 2021). Hygroscopicity measures how much water particles can absorb under specific conditions. It significantly affects the transport and deposition of inhaled aerosols (Darquenne et al., 2016; Davidson et al., 2017; Haddrell et al., 2014). Several techniques are used to investigate the hygroscopic properties of airborne aerosol particles. Some of these include the Humidity Tandem Differential Mobility Analyzer (H-TDMA) (McMurry and Stolzenburg, 1989; Swietlicki et al., 2008; Wang et al., 2018; Wu et al., 2013), Optical techniques like Cavity Ring-Down Spectroscopy (Atkinson et al., 2015; Brock et al., 2016; Langridge et al., 2011; Zhang et al., 2014), Gravimetry techniques (Hitzenberger et al., 1997; Speer et al., 1997) etc. Only limited studies investigate the impact of ambient particle hygroscopic growth on particle lung deposition through direct hygroscopicity measurements. In particular, a single study has reported size-resolved particle hygroscopicity obtained from a high-humidity tandem differential mobility analyzer (HH-TDMA; Relative humidity, RH = 98 %) under conditions similar to those found in the human respiratory tract (Man et al., 2022). This study quantified the combined effects of hygroscopicity and external mixing state on particle deposition in the respiratory tract using the Multiple-Path Particle Dosimetry (MPPD) model. Although this study provides valuable insights by providing size-resolved particle hygroscopicity data at high RH, the scarcity of extremely sensitive HH-TDMA instruments worldwide has led to the predominant use of H-TDMA at 90 % RH in previous research efforts.

The International Commission on Radiological Protection (ICRP 66 recommendations, 1994) and the Multiple-Path Particle Dosimetry (MPPD) model (Asgharian et al., 2001) are the most commonly used dosimetry models. The ICRP model is an empirical model that interpolates experimental data and is a reference. Other deposition models have been developed using a mathematical structure model of the human lung made up of tubes and equations for particle deposition in these tubes by sedimentation, diffusion and impaction, like MPPD and our Hygroscopic Particle Lung Deposition (HPLD) model (Ferron et al., 1988). Estimating the deposition fraction in these models is based on aerosol particle properties and individual physiological parameters. Model estimation commonly overlooks particle hygroscopicity and seldom uses effective density (Lizonova et al., 2024). However, both cause variation in particle size distribution and affect deposition efficiency and pattern for particles in different lung regions. The HPLD model considers the hygroscopic growth of particles and particle density information upon inhalation and is empowered to use various mathematical lung structure models for humans and laboratory animals (Ferron et al., 2013; Schmid et al., 2008).

Previous studies on the impact of hygroscopicity on deposition often relied on assumed values of the hygroscopicity parameter (Kappa, κ), which denotes different particle properties such as non-hygroscopic, nearly hydrophobic, and hygroscopic properties (Voliotis and Samara, 2018) or using estimation by parametric methods (Ching and Kajino, 2018; Haddrell et al., 2015; Hussein et al., 2013; Vu et al., 2018). However, it is widely recognized that ambient aerosol particles typically show an external mixing state and size-dependent hygroscopicity (Zong et al., 2022). Consequently, direct measurement of particle hygroscopic growth is essential to accurately capture the real-time dynamics of hygroscopic growth in the respiratory tract (Man et al., 2022).

In the present study, we use particle properties such as particle number size distribution, density, and hygroscopicity from a measurement campaign in Delhi, India, to model the deposition of inhaled airborne particles on the inner lung surface area. The effective density defines particle mass and influences the HPLD model deposition. Particle hygroscopicity is necessary for accurate deposition assessment (Ferron et al., 1988a,b; Ferron et al., 2013; Karg et al., 2020). The new parameter, “lung tissue deposition”, extends the atmospheric particle measurement results to a toxicological exposure metric. We show its variation using data from four investigative cases: biomass burning episodes, chloride epsiodes (industrial and waste burning), *HOA* dominant episodes (or vehicular emission), and relatively clean periods. While air quality measurement campaigns focus mainly on parameters such as particle number concentration, size distribution and mass concentration to assess the health effects of ultrafine and fine particles, we propose to develop this approach further. We believe that modelling the number and mass of particles delivered to cells within the inner lung tissue is a step forward in interpreting atmospheric measurement data. Adding tissue deposited number and mass to the set of parameters available for correlation with oxidative potential and health effects may provide more substantial and better correlation results than using airborne concentration alone. Deposited number and mass are considered in terms of deposition function, flow rate, and internal lung structure, and their quantification allows direct comparison with results from laboratory exposure studies. We acknowledge that our examples may not fully capture the variability on a national or global scale. Nevertheless, our results highlight that both particle density and hygroscopicity are critical parameters for deposition modelling. Therefore, these properties should be included in the parameter set for future atmospheric measurement campaigns.

To the best of our knowledge, our study represents the first attempt to quantify the effect of particle number size distribution, density and hygroscopicity on lung tissue exposure during different investigative cases in a polluted environment.

2. Materials and methods

2.1. Measurement site

Delhi experiences a wide range of variations in temperature (T), relative humidity (*RH*), wind speed and rainfall over the year and by time of day. Winters (December to February) are cold (T∼10-20 °C mean diurnal range) and humid (*RH* ∼45 % –90 %) with low wind speeds (∼2–3 m s^{-1}). Delhi often experiences shallow inversion layers (depth < 100 m) during winter, especially during the night and early morning hours (Gani et al., 2019). The significant sources of air pollution during the winter season are residential biomass burning, trash burning, industrial activities and vehicular emissions (Mandariya et al., 2024). To investigate Delhi’s ambient air, we installed a suite of online aerosol instrumentation at the Indian Institute of Technology Delhi (IITD) (28.54° N, 77.19° E) from 1 February 2020 to 20 March 2020 (Mandariya et al., 2024; Romshoo et al., 2024). The nearest source of local emissions is two motorways (Shaheed Jeet Singh Marg, about 150 m, and Sri Aurobindo Marg, about 800 m east of the sampling site) and the densely populated residential areas within a 1 km radius. Small and medium-sized industries surround the sampling site within a radius of 25 km that are involved in metal processing, paper production, plastic and pharmaceutical manufacturing, e-waste handling and recycling (Gunthe et al., 2021).

2.2. Instrumentation and data analysis

Hygroscopicity and size distribution data are taken from the measurement campaign from 5 February 2020 to 15 March 2020 using a Humidified Tandem Differential Mobility Analyzer (H-TDMA; TROPOS Germany) and a TROPOS-type Mobility Particle Size Spectrometer (MPSS; TROPOS, Germany) respectively (Mandariya et al., 2024). The H-TDMA system has been used previously in numerous field campaigns (Massling et al., 2007; Wu et al., 2013; Zhang et al., 2016). This system consists of two Hauke-Median Differential Mobility Analyzers (DMAs), a Condensation Particle Counter (CPC; TSI Model 3772), and a humidifier system between the two DMAs. The H-TDMA system measured the particle's hygroscopic growth factors (HGFs) with D_p dry at five different sizes (20, 50, 100, 150 and 200 nm) at 90 % *RH*. A full scan covering all five sizes had a time resolution of approximately 30 min. The size distributions were measured using a TROPOS-type MPSS (in the size range of 10–800 nm) (Wiedensohler et al., 2012) consisting of an electrostatic classifier, a differential mobility analyzer, a Kr- 85 bipolar charger, and a condensation particle counter (CPC; TSI Model 3076).

In addition, an aerosol chemical speciation monitor (ACSM; Aerodyne USA) was operated to provide the bulk chemical composition of atmospheric aerosol particles. On ACSM data, we performed a positive matrix factorization resulting in a four-factor solution: hydrocarbon-like organic aerosol (*HOA*), biomass-burning organic aerosol (*BBOA*), less oxidized oxygenated organic aerosol (*LO-OOA*), and more oxidized oxygenated organic aerosol (*MO-OOA*). Further details on the operation of the ACSM, calibration, data analysis, etc., can be found in (Mandariya et al., 2024). The particle density data for the current study was derived from the ACSM data (Sup. Table S1) following Eq. (1).

2.3. Pollution cases

From the comprehensive campaign dataset, data on concentration, composition, wind direction, and other relevant factors were extracted and organized into three representative scenarios. As previously mentioned, these scenarios correspond to PMF factors obtained on the ACSM dataset: *BBOA* and *HOA*, which are typically associated with biomass burning and vehicular emissions, respectively. Additionally, chloride was selected as the inorganic species identified by ACSM. Furthermore, relatively clean periods were included, with all four collectively referred to as "investigative cases." To be more precise, the pollution cases were characterized by i) high concentrations of biomass burning aerosols (*BB*), ii) high concentrations of chloride aerosol from industrial processes and waste burning (*Cl*), and iii) high concentrations of hydrocarbon-like organic aerosol (*HOA*) from vehicular emissions. Data sets with relatively clean periods (*RC*) were selected for comparison (Mandariya et al., 2024). The "investigative cases" data are also analyzed for the day and nighttime separately: Data with a timestamp from 8 am to 8 pm were considered as "day", and data with a timestamp from 8 pm to 8 am the next day as "night". The time series of all-important aerosol parameters and the assignment to the "investigative cases" can be found in Mandariya et al., (2024).

2.4. Particle density

The particle effective density ρ_p is required to estimate particle mass from number size distribution. We use the equation of Zhou et al., (2022) to estimate ρ_p from the chemical species' (*j*) mass fraction data $mf_{j,\,ACSM}$ and their respective bulk density ρ_j. This study calculated the effective density using the equation described below based on ACSM data. The approach of utilizing a single characteristic density value for each investigative case presents both advantages and limitations. By defining density as an independent variable, not contingent on particle diameter, this method streamlines the modelling process and enables the differentiation between distinct cases. However, this assumption introduces a degree of uncertainty, as it fails to consider potential variations in density across different particle sizes, which could affect the accuracy of the model's output. We have also tried an alternative approach to utilize size-resolved density data, as exemplified by the same publication, i.e. Zhou et al. (2022), which offers a more granular methodology that could enhance our model simulations with detailed size-dependent density information. While using the size-dependent density information retrieved from the Beijing data could offer insights into size-resolved characteristics, it may not represent four different investigative cases, as it does not fully account for how density variations impact the outcomes across different investigative cases. To reduce uncertainties and enhance model precision, measuring size-resolved density directly in the field during campaign studies is recommended, providing a more comprehensive representation of the density variability across particle sizes.

$$\frac{1}{\rho_p} = \sum_{j=1}^{N} \frac{mf_{j,ACSM}}{\rho_j} \tag{1}$$

For comparison, all model calculations are performed for non-hygroscopic unit density ($\rho_0 = 1\ \mathrm{g\ cm^{-3}}$) particles (*nhp*) additionally. The ratio $\rho_p\ /\ \rho_0$ is constant during an investigative case. A sensitivity study is performed to determine the influence of different particle densities on lung tissue deposition (Sup. Fig. S4).

ρ_p is used for the mass calculation and lung deposition modelling, as there is no direct measured size-resolved density information from the campaign dataset. The mean composition of the particles during the respective observation case was used for the modelling. This is a crude assumption, but only particle-volume size distribution can be calculated without any density information. The lung-deposited volume, however, has not been interpreted by toxicologists so far.

2.5. Particle mass

The airborne particle-mass size distribution (C_m) is derived from the particle-number size distribution (C_n) using ρ_p (Schmid et al., 2007; Zhou et al., 2022). When atmospheric background particles commonly undergo ageing processes during transport, their form factor is close to 1. For the aggregated ultrafine particles, information about the form factor would be helpful, but is less important as the contribution to particle mass concentration is low (see supplement). C_m is calculated channel-wise from C_n for each diameter D_p (diameter of dry particles) by

$$C_m = C_n \frac{\pi}{6} \rho_p D_p^3 \tag{2}$$

2.6. Particle hygroscopicity

Hygroscopic particles (*hp*) grow until equilibrium is reached between the vapour pressure across their curved surface and the surrounding air, typically quantified by relative humidity (*RH*) (Man et al., 2022; Mandariya et al., 2024, 2020). This growth process is characterized by the growth factor (*GF*), defined as the particle diameter ratio at a given RH to its initially dry diameter (Mandariya et al., 2024, 2020). During the Delhi campaign, conducted using an H-TDMA, particle size was measured in the first differential mobility analyzer (DMA 1) under dry conditions and after that in DMA 2 under $RH = 90$ % (Mandariya et al., 2024). All growth factors discussed here are relative to this specific humidity condition.

Perwitzschky, (1928) documented that the lungs' relative humidity (*RH*) reaches 98 % and 99.9 %. Consistent with previous studies (e.g., Vu et al., 2015), an *RH* value of 99.5 % was used to represent lung conditions.

The Rissler approximation ((Farkas et al., 2020; Kristensson et al., 2013; Rissler et al., 2006) was used to estimate particle diameters at this *RH*:

$$HGF(99.5\%) = \left[1 + \left(HGF(a\%)^{3} - 1\right) \times \frac{(99.5\% - a\%)}{100} \times exp\left(-Dp \times \frac{(HGF(99.5\%) - 99.5\%)}{100}\right) \times exp\left(-Dp \times \frac{(HGF(a\%) - a\%)}{100}\right)\right]^{\frac{1}{3}} \quad (3)$$

HGF (99.5 %) is the hygroscopic growth factor at an *RH* of 99.5 %. $HGF(a\%)$ represents the growth factor at an arbitrary *RH* ($a\%$) and *Dp* is the dry particle diameter. This equation simplifies the adaptation of the classical Köhler theory. For our analysis, the parameter $a\%$ was set at 90 %.

The H-TDMA can measure *GF* up to 200 nm; however, the upper size limit of our DMA is 837 nm. No data regarding the hygroscopic nature of the particles is available for the surplus range; therefore, the 200 nm value has been selected for substitution. The assumption that the *GF* for particles larger than 200 nm remains consistent with that of 200 nm-sized particles introduces some limitations. Still, it is justifiable, given the constraints and context of the study. The key limitation is that this assumption may only partially capture potential size-dependent variations in composition and hygroscopicity beyond 200 nm, particularly for particles influenced by distinct emissions or atmospheric processes. For example, larger particles may incorporate different chemical species through aging or mixing processes that could affect their hygroscopic properties. However, the justification for this simplification lies in several factors.

First, the *GF* values at 200 nm are within a range that aligns with atmospheric observations, and these values represent a reasonable approximation for accumulation mode particles, which tend to have a relatively homogeneous composition due to their longer atmospheric lifetimes and mixing processes. Second, the lack of direct hygroscopicity measurements above 200 nm necessitates some extrapolation or substitution to maintain model functionality. Third, the HPLD model's reliance on *GF*, rather than κ values, precludes a straightforward conversion of existing hygroscopicity data into κ-derived inputs. This methodological limitation emphasizes the need for consistency in input parameters, further supporting the decision to use 200 nm *GF* as a proxy for larger particles.

Future work could address these limitations by fine-tuning the HPLD model to accept κ values as input, enabling integration of κ-derived data for larger particle sizes. This would allow the incorporation of ACSM-derived κ values, potentially improving model accuracy for particles > 200 nm. Nevertheless, given the current model structure and available data, the assumption is reasonable and minimizes the introduction of speculative uncertainties while maintaining alignment with observed atmospheric particle properties. Upon inhalation, particles experience an immediate growth in the respiratory system. The study by Ferron et al., (2013) suggests that the inhaled air reaches equilibrium relative humidity (*RH*) after passing through the nose, trachea, and particularly beyond lung generation 4 (Morawska and Buonanno, 2021). The RH in the lung is maintained at approximately 99.5 % due to the isotonic properties of blood, which Scientific Tables Geigy has reviewed (Peppas, 1984). These tables are cited by many studies (Ferron et al., 1988a,b; Petters and Kreidenweis, 2007). The final size of hygroscopic particles determines their deposition site. It is independent of their airborne size and *RH* before inhalation, as they always grow rapidly to an *RH* of 99.5 %. Compared to the amount of condensing water needed for particle growth, the reservoir for water vapor provided by the lung is considered infinite. Consequently, the *RH* of the atmosphere outside the respiratory tract hardly influences lung deposition and is not to be considered here for hygroscopic growth modelling.

Additionally, modern particle sizing instrumentation is commonly supplied with compressed clean air to prevent internal condensation and to avoid ambient temperature and humidity influencing the sizing results. Hence, the measured airborne particle diameter given in the literature is commonly a "dry diameter," our modelling results for *hp* are compared in addition to that.

2.7. The hygroscopic particle lung deposition model

The Hygroscopic Particle Lung Deposition (HPLD) model (Ferron et al., 2013) provides data on particle deposition (*DE*) for both hygroscopic (*hp*) and non-hygroscopic (*nhp*) particles. The HPLD model has been extensively described in the literature, including by Ferron et al. (2013), Ferron et al. (1988a), Ferron et al. (1988b), and Schmid et al. (2008).

For a more realistic breathing situation, the model has been improved. Karg et al., (2020) utilized the HPLD model to estimate the tissue-deposited particle number (TD_n) and mass (TD_m) and compared these results with laboratory cell exposure experiments. In comparison to models such as the Multiple-Path Particle Dosimetry (MPPD) model (Asgharian et al., 2001) and the stochastic model (Hofmann, 2006), a notable advantage of the HPLD model is its ability to provide data on the hygroscopic growth of particles during the particle transportation to the inner lungs. The HPLD model can accommodate a wide range of lung structures and breathing parameters due to its utilization of deposition equations for tubular flow. Moreover, it has been demonstrated to apply to laboratory animals, including rats (Ferron et al., 2013). Here, we use a mathematical structural model of the human lung as described by Yeh and Schum (1980). This structural framework describes the lung as an assembly of hierarchically organized tubes, each bifurcating into two equivalent daughter tubes of identical dimensions in length and diameter and inclined at a given angle to each other and gravity. Tubes with identical geometric characteristics are classified within the same lung generation. The structural configuration includes 24 tube generations, ending in the alveolar sacs. The framework used here represents the lung structure of an adult man. It is extended by a nose/ mouth and a pharynx, adding up to 26 lung generations by Ferron et al., (2013). The oral cavity and oropharynx are set as generations 1 and 2, respectively, the trachea as generation 3, the bronchi as generations 4 to 9, the bronchioles as generations 10 to 19, and the alveolar ducts as 20 to 26. Instead of using the lung volume of 5,564 cm^3 proposed by Yeh and Schum, (1980), we adopt a more realistic value. This updated lung volume is calculated as the sum of the functional residual capacity (3300 cm^3). This is in line with the recommendation by the International Commission on Radiological Protection (ICRP 66 recommendations (1994)) supplemented by adjusting 50 % of the tidal volume (equivalent to 50 % of 750 cm^3). The HPLD model describes *DE* by mechanisms including diffusion, sedimentation within a stable laminar flow regime, and impaction across each lung generation. In particular, deposition within ducts containing alveoli shows a remarkable correlation with alveolar diameter.

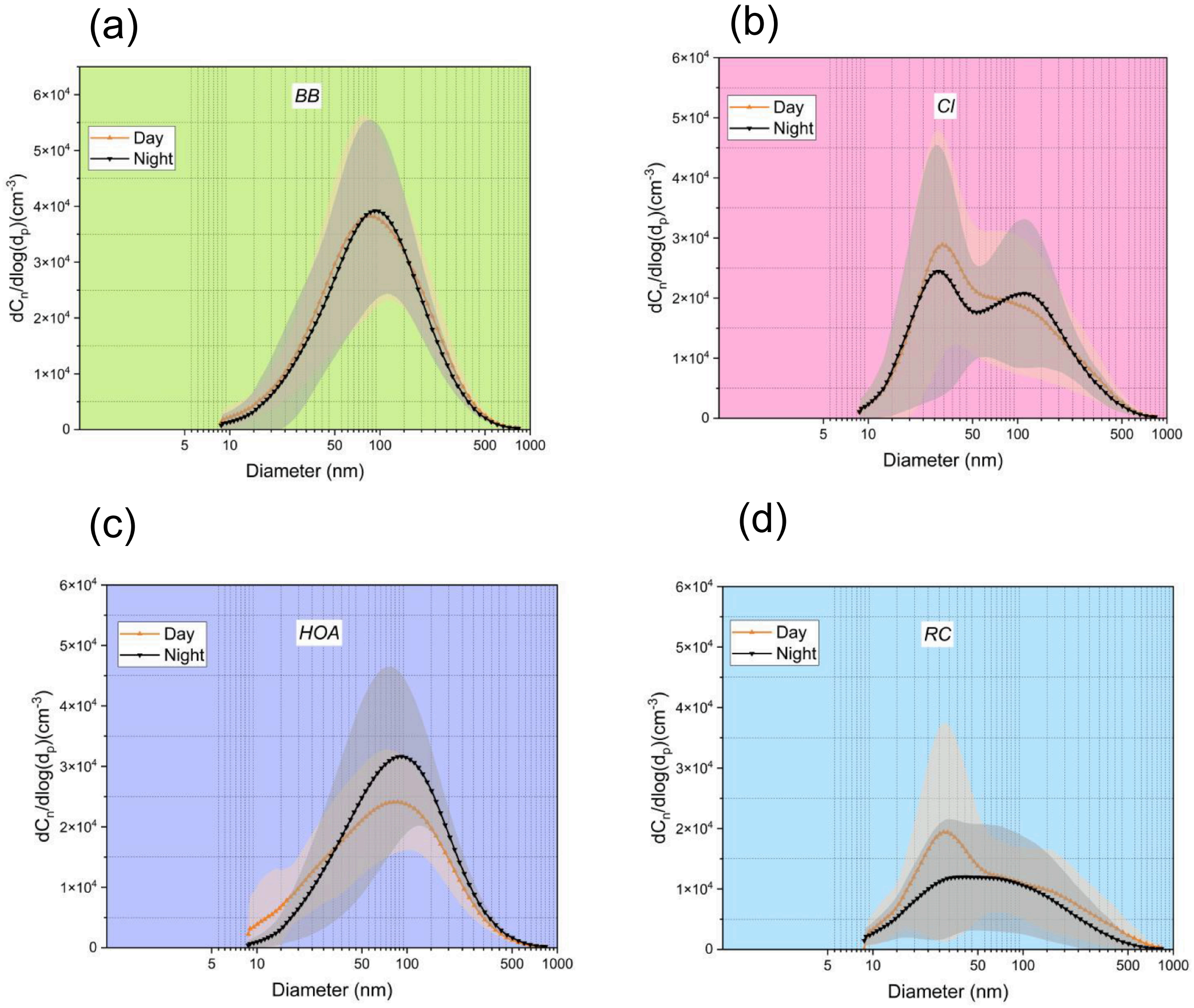

Fig. 1. Measured airborne particle number size distribution C_n during all investigative cases: (a) biomass-burning organic aerosol (BB), (b) high concentration of chloride aerosol (due to emissions from industries and trash burning) (Cl), (c) high concentration of hydrocarbon-like organic aerosol from vehicular emission (HOA), and (d) periods with relatively clean air (RC). The graphs show the channel-wise averaged concentration and standard deviation between 8 am and 8 pm (daytime, orange line) and between 8 pm and 8 am of the next day (nighttime, black line). The shaded area represents the standard deviation of the number concentration (#/cm^3) in each size bins. (For interpretation of the references to colour in this figure legend, the reader is referred to the web version of this article.)

2.8. *Estimation of tissue deposited particle number and mass*

Tissue deposited (*TD*) particle number and mass (TD_n and TD_m, respectively) are toxicologically relevant parameters. *TD* represents the toxicological burden for epithelial lung tissue over a defined time. *TD* considers all the processes a particle goes through until it reaches a cell surface. Biologists and toxicologists can utilize this information to discuss the subsequent biological processes of dissolution, translocation and cellular or systemic defense elsewhere. TD_n and TD_m are calculated here for three lung regions (*R*) and the sum of internal surface area of all three lung regions (total lung surface area, *TLSA*). The internal surface area of the extra-thoracic (*EX*), tracheobronchial (*TB*) and alveolar (*AL*) lung regions is covered by different epithelial cell types. It represents different proportions of the total lung surface (Karg et al., 2020). *TD* is calculated from the HPLD output using an internal lung surface area (A_R) of 0.09, 0.33, 74.6 and 75 m^2 for *EX*, *TB*, *AL* and *TLSA*, respectively. Respiratory parameters are for a person sitting at rest (750 cm^3 tidal volume, 12 breaths per minute) (Ferron et al., 2013) breathing permanently with an identical in and exhalation flow rate and with no pause in between.

TD factors (TD_f) are calculated from the HPLD-deposition data (*DE*) (Eq. (4) using the respiratory flow rate (*Q*), exposure time (t_e) and regional lung surface area (A_R). *DE* itself depends on the lung region *R* and the aerosol parameters D_p, ρ_p and *GF*:

$$TD_f(R, D_p, \rho_p, GF) = Qt_e\frac{DE(R, D_p, \rho_p, GF)}{A_R} \tag{4}$$

This means the TD_f is already the modelling output. Obtain TD_n or TD_m by the channel-wise multiplication (convolution) with the airborne number concentration (C_n) or the airborne mass concentration (C_m):

$$TD_n(R, D_p, \rho_p, GF) = C_n(D_p)TD_f(R, D_p, \rho_p, GF) \tag{5a}$$

$$TD_m(R, D_p, \rho_p, GF) = C_m(D_p)TD_f(R, D_p, \rho_p, GF) \tag{5b}$$

In other words, the TD_f comprises the whole modelling process and can be modelled in an extra process without using the airborne distribution. Modelling the TD_f includes the breathing parameters (Q, t_e, A_R) and the particle parameters (D_p, ρ_p, *GF*) but not the airborne data (C_n, C_m). The TD_f used for our investigative cases is tabled in the supplement and can readily be used to estimate TD_n and TD_m for other measurement campaigns with similar investigative cases without running the HPLD model.

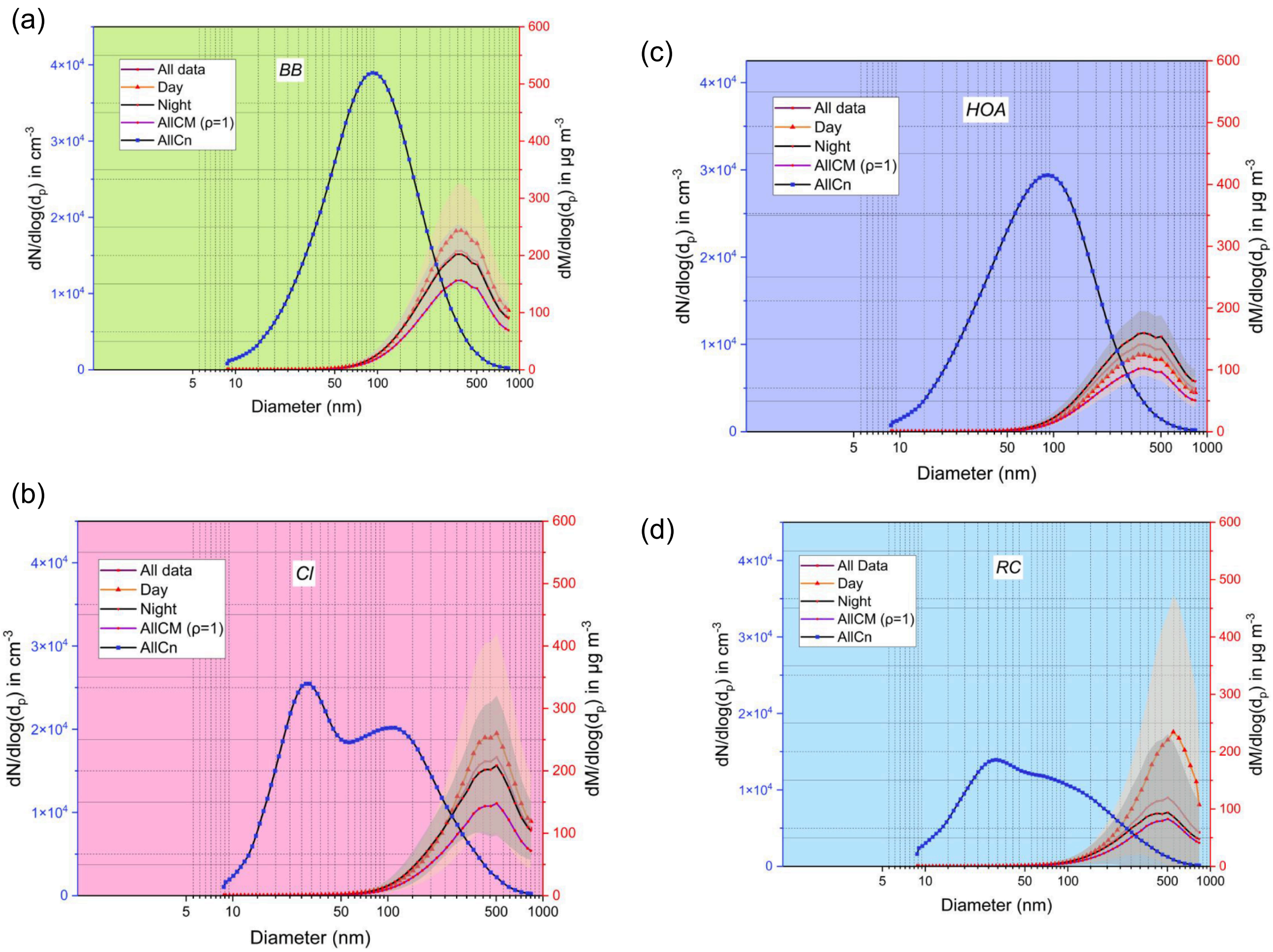

Fig. 2. Airborne particle mass distribution during all investigative cases (a) biomass-burning organic aerosol (BB), (b) high concentration of chloride aerosol (due to emissions from industries and trash burning) (Cl), (c) high concentration of hydrocarbon-like organic aerosol from vehicular emission (HOA), and (d) periods with relatively clean air (RC). Distributions are calculated from airborne particle number size distributions (Fig. 1) using the particle density listed in Table 2 for BB, Cl, HOA and RC cases. Day- and nighttime averaging is identical with Fig. 1. Both the mass distribution for non-hygroscopic unit-density particles (allCM(ρ = 1)) and particle number size distribution (allCn) are added for comparison. The shaded area represents the standard deviation of the number concentration (#/cm^3) in each size bins.

This implies that the model TD_f can be generated using typical breathing parameters and particle properties. It can then be applied to calculate TD from atmospheric or laboratory particle distributions, provided that the ρ_p and GF data are compatible.

3. Results and discussions

3.1. Estimation of particle density for calculating mass distribution and lung deposition

Table 2 provides the densities calculated for the investigative cases. Aerosol densities have been reported to range from 1.3 to 1.6 g cm^{-3} (Hu et al., 2012; Sarangi et al., 2016). Another study in Delhi determined aerosol mass based on particle size distribution observations by applying a density of 1.7 g cm^{-3} (Laakso et al., 2006).

Since non-hygroscopic combustion emissions predominate in both biomass burning aerosol (*BB*) and hydrocarbon-like organic aerosol (*HOA*) from vehicular emissions, the particle densities for these episodes were lower than for the chloride emission particles (*Cl*) and the relatively clean episode particles (*RC*). Freshly emitted combustion emission particles hardly contribute to C_m as they are ultrafine ($\leq$100 nm) or nano-sized and as their density is low (see supplement Section 2). The main contribution to particle mass comes from fine particles (>100 nm), i.e. from the "tail" of the measured number size distribution (Figs. 1 and 2). Details about the sensitivity of TD to particle density are given in Fig. S4 in the supplement.

3.2. Airborne size distribution of particle number and mass concentration required for the lung deposition calculations

Regarding the four investigative cases, *BB*, *HOA*, *Cl*, and *RC*, Fig. 1 and Table 2 present the measured airborne size distributions of particle number concentrations (Mandariya et al., 2024). The shapes and concentrations of these distributions vary. The ultrafine particle (UFP) concentration is primarily attributed to freshly emitted combustion particles (Kwon et al., 2020). The order of the investigative cases by number concentration is as follows: $BB > Cl > HOA > RC$. The number concentration during *BB* emissions is twice that of the *RC* period. The mass distribution graphs in Fig. 2 are incomplete because they stop at the upper sizing limit of the MPSS particle sizer (836 nm). The missing particle mass concentration ranges from 7 % to 24 % (Sup. Section 1). Despite that, the mass size distributions are used here, as i) the distributions can be completed by fitting lognormal distributions, ii) the mode of all distributions is accessible, iii) the integral of a lognormal distribution is directly related to the mode (median) value (see supplement Section 1.1), and iv) the order of the investigative cases is unchanged

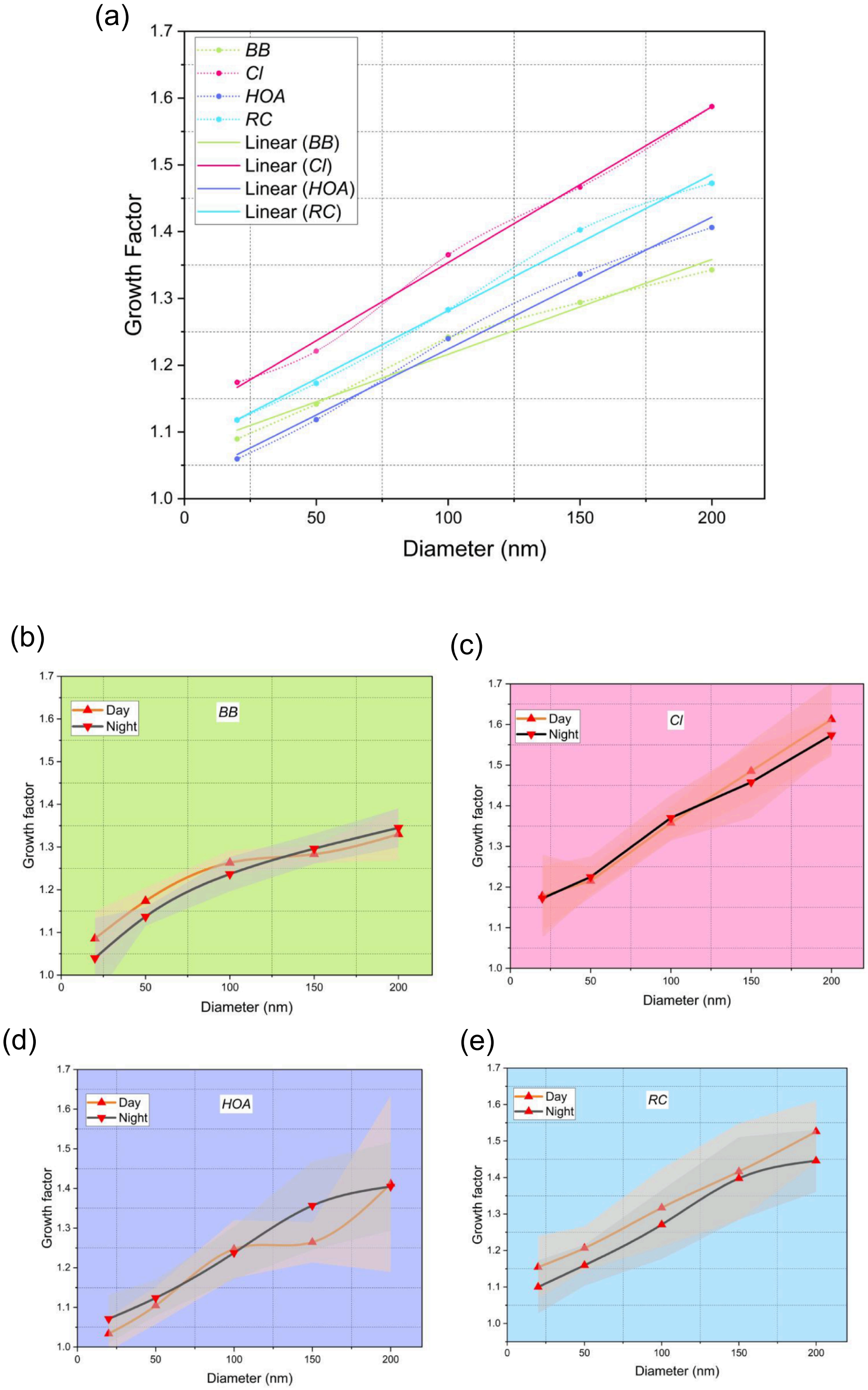

Fig. 3. Measured growth factors (GF) during all investigative cases (as indicated in Fig. 1). (a) GF characterizes the size dependency of particle hygroscopicity. It is fitted with a linear function (dashed lines) for better use in the HPLD model (find the fit parameters in Table 1). The slopes of the fits vary from 1.45 to 2.27 μm^{-1}, and the intercepts from GF = 1.02 to GF = 1.13. The correlation coefficient is close to R^2 = 1 for all fits. Hygroscopic growth factors at day- (orange lines) and night-time (black lines) during all investigative cases: (b) biomass-burning (BB), (c) chloride (Cl), (d) vehicular emission (HOA), and (e) relatively clean (RC) periods. The shaded area represents the standard deviation. (For interpretation of the references to colour in this figure legend, the reader is referred to the web version of this article.)

when completed mass distributions are used.

The four case's total mass concentration is between 60 and 133 μg m^{-3} (Table 2, "All data"). The mass concentration order is identical to the number concentration order (*BB* > *Cl* > *HOA* > *RC*). Total mass concentration is relatively high for all cases, characterizing Delhi as a highly polluted place. Particle mass is modelled using the effective density. It yields a 30 to 50 % higher exposure concentration than particle mass from ρ_0 (Table 2). This is an argument to measure particle

Table 1
Growth factor fit parameters for all investigative cases. Growth factors (GF) are fitted to the hygroscopicity data (Fig. 3) by straight lines with a slope (parameter a, in Eq. (6) and intercept (parameter b, in Eq. (6). R^2 is the coefficient of determination, Avg. the average of all investigative cases, S.D. the corresponding standard deviation, and C.V. the coefficient of variation. For comparison, the ratio to the relatively clean case *RC* is given for each slope, intercept and R^2.

Case / Statistics	Measured GF		Linear fit parameters		
	Minimum	Maximum	Slope	Intercept	R^2
BB	1.09	1.34	1.42	1.07	0.97
Cl	1.17	1.59	2.34	1.12	1
HOA	1.06	1.41	1.98	1.03	0.99
RC	1.12	1.47	2.04	1.08	0.99
Avg.	1.11	1.45	1.94	1.07	
S.D.	0.05	0.1	0.38	0.04	
C.V. in %	7.2	4.39	19.7	3.5	
BB/RC	0.97	0.91	0.7	1	0.98
Cl/RC	1.04	1.08	1.14	1.04	1
HOA/RC	0.94	0.95	0.97	0.95	1

Table 2
Average airborne particle number (C_n) and mass-concentration (C_m) during all investigative cases. Average and standard deviation (S.D.) are given separately for the total investigative case (all data) and day and nighttime. C_m is calculated channel-wise from C_n. Data are calculated for non-hygroscopic dry particles (*nhp*) using unit density ρ_0 and hygroscopic particles (*hp*) at RH = 90 % using the density ρ_p of the respective case. Additionally, the ratio of day vs nighttime is given. The ratio is > 1 if the concentration is higher during daytime and < 1 if it is higher during nighttime.

Case	All data	± S.D.	Daytime	± S.D.	Nighttime	± S.D.	Day: Night
Particle number concentration C_n (x 10^4 cm^{-3})							
BB	3.24	1.91	3	1.33	3.29	1.48	0.91
Cl	2.58	1.68	2.79	1.65	1.85	1.71	1.51
HOA	2.57	1.24	2.29	7.92	2.7	1.35	0.85
RC	1.5	1.22	1.81	1.33	1.37	1.11	1.32
Non-hygroscopic particle mass concentration (C_m, ρ_0) in µg m^{-3})							
BB	95.8	44.8	134	42	93.4	24.9	1.44
Cl	79.3	42.5	108	56	56	41.3	1.93
HOA	66.9	18.9	82.2	20	67.4	19.9	1.22
RC	43	48.9	72.9	68	36.2	44.4	2.01
Hygroscopic particle mass concentration (C_m, ρ_p) in µg m^{-3})							
BB (ρ_p = 1.33)	127	60	179	56	124	33	1.44
Cl (ρ_p = 1.50)	119	64	162	84	84	62	1.93
HOA (ρ_p = 1.38)	92.4	26	113	27	93.1	27	1.22
RC (ρ_p = 1.45)	62.3	71	106	98	52.5	64	2.01

density during field campaigns.

3.3. Hygroscopicity

The growth of hygroscopic particles during the four investigating cases is depicted in Fig. 3. As particle size increases, so do all growth factors (*GF*). Fig. 3a shows the *GF* for the average data, and Fig. 3b-e shows the *GF* for the day and night data. To easily address *GF* (D_p) during the modelling process, a straight line fitting was applied. It should be noted that *GF* is influenced by both curvature and chemical composition; therefore, it is non-linear with particle size. The fitting is restricted to the displayed size range (25 to 200 nm), and extrapolation may yield spurious results. Nevertheless, the coefficient of determination is high ($0.98 \leq R^2 \leq 0.99$; see Fig. 3a and Table 1), and the fits may help to describe the data more easily:

$$GF(D_p) = aD_p + b \quad (6)$$

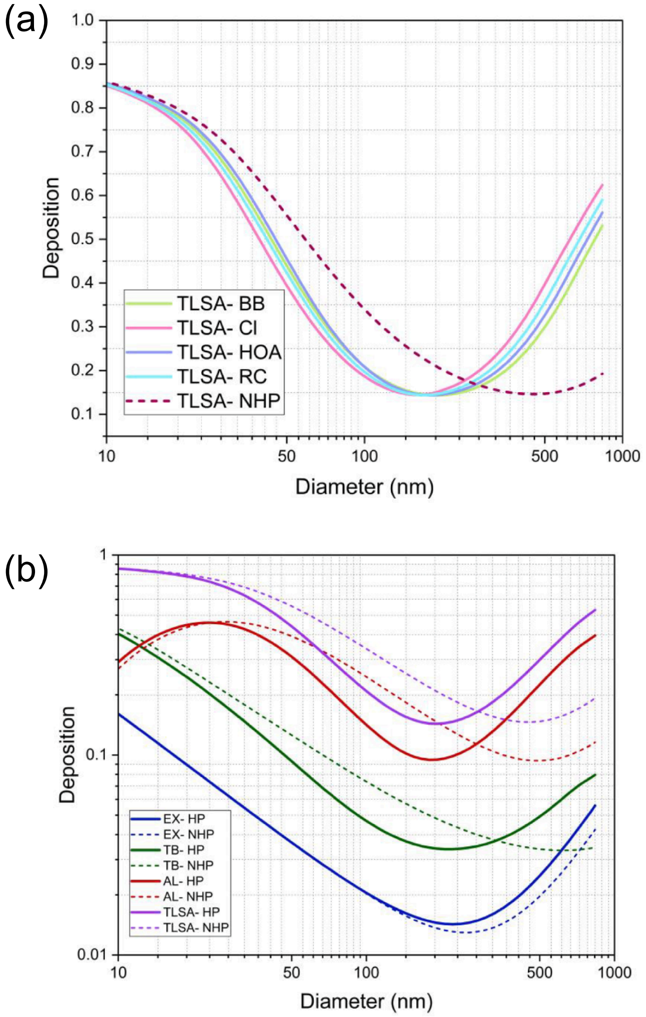

Fig. 4. a) deposition in the total lung surface area during the episodes (BB – green dashed line, Cl – pink dash-dotted line, HOA – purple dash-double-dotted line, RC – blue solid line), and for non-hygroscopic particles (nhp, red dotted line). the deposition minimum is found at 461 nm for the non-hygroscopic particles and at 192, 156, 179 and 167 nm for the BB, Cl, HOA and RC cases, respectively. b) Deposition probability for the extra-thoracic (EX), tracheobronchial (TB) and alveolar (AL) lung region and for the total lung surface area (TLSA) for both non-hygroscopic (nhp, dashed lines) and hygroscopic particles (hp, solid lines) during the biomass-burning (BB) case. In EX, TB, AL and TLSA, the mean deposition minimum diameter is found at 259, 602, 503 and 461 nm for nhp, respectively, and 223, 207, 179 and 192 nm for hp, respectively. (For interpretation of the references to colour in this figure legend, the reader is referred to the web version of this article.)

The slope (*a*) is between 1.42 and 2.34 μm^{-1} depending on the investigative case, and the intercept (*b*) is between *GF* = 1.03 and 1.12. The lowest *b* is found for *HOA* type aerosol (or dominated by vehicular emissions), as the freshly emitted combustion particles are merely *nhp* (Table 1, Fig. 3a). The highest is found for chloride episodes. Gunthe et al., 2021 reported that chlorine is released from metal processing industries or illegal waste burning activities. It is then "neutralized" by excess ammonia in the atmosphere, forming ammonium chloride (for simplicity, we refer to it as chloride or *Cl*), and is found to be very hygroscopic (Gunthe et al., 2021). The intercept for *RC* is lower (1.08) than for *Cl*. Due to the influence of non-hygroscopic ultrafine emission particles, the lowest intercept is observed for both the *BB* and the *HOA* investigative cases. *BB* has the lowest slope, which results in the lowest hygroscopicity, particularly for particles in the tiny particle size range of

Table 3

Tissue deposited particle number (TD_n) and mass (TD_m), as TLSA modelled for non-hygroscopic particles (nhp) with density ρ_0, and for hygroscopic particles (hp) with the hygroscopic profiles of the investigative cases (see Fig. 3 and Table 1). Deposition data are calculated for the investigative cases: biomass-burning (BB), chloride (Cl), vehicular emission (HOA), and relatively clean period (RC). TD during a case is given for the extra-thoracic (EX), the tracheobronchial (TB), the alveolar (AL) lung region, and the total lung surface area (TLSA). The day- vs. nighttime ratio is given in the column day: night for the total lung. The ratio is > 1 if TD is higher during the day and < 1 if it is higher during the night. The density- and hygroscopic vs. non-hygroscopic modelling ratio for TLSA is given in column r, GF. $TD(r_p)$: $TD(r_0)$ means only particle density is modelled while $GF = 1$. TD(hp): $TD(r_0)$ means that density and hygroscopicity are modelled. The comparative ranking of the investigative cases by TD (TLSA) is given in column Case: RC.

Tissue-deposited particle statistics (TD)

	All data				Day	Night	Day: Night	r, GF	Case: RC
Lung region	EX	TB	AL	TLSA	TLSA	TLSA	TLSA	TLSA	TLSA
Cases	Tissue deposited number TD_n (nhp, ρ_0) in part. $cm^{-2}h^{-1}$						Ratio	Ratio	Ratio
BB	5.83×10^6	5.27×10^5	6.43×10^3	9.42×10^3	1.00×10^4	9.39×10^3	1.07	–	1.69
Cl	6.54×10^6	5.70×10^5	5.93×10^3	9.19×10^3	9.63×10^3	9.04×10^3	1.06	–	1.65
HOA	5.06×10^6	4.54×10^5	5.36×10^3	7.94×10^3	8.11×10^3	8.32×10^3	0.97	–	1.42
RC	4.18×10^6	3.59×10^5	3.52×10^3	5.59×10^3	6.79×10^3	5.01×10^3	1.35	–	1
	Tissue deposited number TD_n (nhp, ρ_p) in part. $cm^{-2}h^{-1}$							$TD_n(r_p)$: $TD_n(r_0)$	
BB	5.92×10^6	5.28×10^5	6.45×10^3	9.45×10^3	1.01×10^4	9.42×10^3	1.07	1	1.69
Cl	6.65×10^6	5.70×10^5	5.95×10^3	9.23×10^3	9.66×10^3	9.08×10^3	1.06	1	1.65
HOA	5.14×10^6	4.55×10^5	5.38×10^3	7.97×10^3	8.13×10^3	8.35×10^3	0.97	1	1.42
RC	4.22×10^6	3.59×10^5	3.53×10^3	5.60×10^3	6.81×10^3	5.03×10^3	1.35	1	1
	Tissue deposited number TD_n (hp, rp) in part. $cm^{-2}h^{-1}$							$TD_n(h_p)$:$TD_n(r_0)$	
BB	5.90×10^6	4.01×10^5	4.92×10^3	7.37×10^3	7.78×10^3	7.40×10^3	1.05	0.78	1.55
Cl	6.62×10^6	4.22×10^5	4.87×10^3	7.50×10^3	7.90×10^3	7.34×10^3	1.08	0.82	1.58
HOA	5.12×10^6	3.60×10^5	4.26×10^3	6.44×10^3	6.82×10^3	6.66×10^3	1.02	0.81	1.36
RC	4.21×10^6	2.84×10^5	3.00×10^3	4.74×10^3	5.76×10^3	4.31×10^3	1.34	0.85	1
	Tissue deposited mass TD_m (nhp, ρ_0) in pg $cm^{-2}h^{-1}$								
BB	1.06×10^4	6.51×10^2	8.48	1.26×10^1	1.85×10^1	1.63×10^1	1.13	–-	2.32
Cl	9.26×10^3	5.14×10^2	6.64	9.98	1.62×10^1	1.45×10^1	1.12	–-	1.85
HOA	7.48×10^3	4.59×10^2	5.99	8.88	1.05×10^1	1.45×10^1	0.73	–-	1.62
RC	5.09×10^3	2.77×10^2	3.57	5.39	1.28×10^1	6.68	1.92	–-	1
	Tissue deposited mass TD_m (nhp, ρ_p) in pg $cm^{-2}h^{-1}$							$TD_m(r_p)$:$TD_m(r_0)$	
BB	1.66×10^4	8.74×10^2	1.17×10^1	1.75×10^1	1.47×10^1	1.29×10^1	1.14	1.4	2.06
Cl	1.85×10^4	7.96×10^2	1.09×10^1	1.65×10^1	1.20×10^1	1.07×10^1	1.13	1.66	1.95
HOA	1.26×10^4	6.36×10^2	8.63	1.29×10^1	8.18	1.05×10^1	0.78	1.48	1.52
RC	9.38×10^3	4.12×10^2	5.58	8.5	9.77	4.99	1.96	1.58	1
	Tissue deposited mass TD_m (hp, ρ_p) in pg $cm^{-2}h^{-1}$							$TD_m(h_p)$:$TD_m(r_0)$	
BB	1.68×10^4	9.28×10^2	1.62×10^1	2.22×10^1	2.49×10^1	2.18×10^1	1.14	1.78	1.62
Cl	1.85×10^4	1.07×10^3	2.11×10^1	2.79×10^1	3.21×10^1	2.65×10^1	1.21	2.8	2.03
HOA	1.25×10^4	6.98×10^2	1.25×10^1	1.70×10^1	1.50×10^1	1.95×10^1	0.77	1.94	1.24
RC	9.64×10^3	5.33×10^2	1.03×10^1	1.37×10^1	2.66×10^1	1.02×10^1	2.62	2.55	1

150 and 200 nm. The graphs demonstrate that the *nhp* emissions during *BB* are larger than those during *HOA*, which commonly come from fuel injection engines and are in the ultrafine range (≤100 nm).

Fig. 3 b-e shows hygroscopicity by day and night. Both during the day and at night, hygroscopicity increases with particle size. Although evident in the data, day-night differences are rarely statistically distinguishable. Differences are more prominent between the episodes. Hygroscopicity tends to be slightly lower during the daytime. Hygroscopicity is reduced at night just for *RC*. This can be explained by relatively enhanced ultrafine (≤100 nm) C_m traffic combustion emission at night or a decreased dilution due to tropospheric vertical mixing.

Cl exhibits the highest hygroscopicity among all the investigative cases (Fig. 3c). Hygroscopicity, in this case, is almost the same at night and during the day. Hygroscopicity is increased due to hygroscopic compounds, particularly those in particles with sizes between 150 and 200 nm. During *HOA*, the daytime and nighttime data sets exhibit a comparable slope and nearly the same low hygroscopicity (Fig. 3d). During the day, a C_m particle source appears to reduce hygroscopicity, particularly for 150 nm particles. At night, hygroscopicity for *HOA* is lower than for night *RC*. The high day and evening traffic emissions could explain this reduction. For the investigative case, *RC*, the nighttime *GF* is lower than the daytime *GF* for all the particle sizes. Reductions in ageing time, secondary background aerosol levels (expected to be lower on cleaner days), and dilution through tropospheric vertical convection at night significantly reduce hygroscopicity.

3.4. Lung deposition calculation using the HPLD model

The deposition in the total lung surface area for the four investigative cases is presented in Fig 4b, which also shows the *DE* of the different lung regions for both *hp* and *nhp*. While deposition by both gravitational and inertial transport increases with particle diameter ('aerodynamic regime'), deposition by diffusive transport (Brownian motion, $D_p \leq 200$ nm for hp, $D_p \leq 400$ nm for *nhp* in Fig 4 a) decreases with increasing particle diameter. Both superposition regimes form the well-known "U-shaped" deposition function with its characteristic minimum.

DE in the total lung (Fig 4 a) shows slight but distinguishable differences between the four investigated cases. Due to their low hygroscopicity, *BB* particles show the deposition minimum at the largest diameter (192 nm). In contrast, most hygroscopic *Cl* particles show the deposition minimum at the smallest diameter (167 nm). For *nhp*, the deposition minimum is found at 462 nm. A more significant "shift" to lower diameters is observed for particles containing more hygroscopic substances. However, the "hygroscopic shift" between *nhp* and *hp* (462 nm to 192 nm) is much greater than the "shift" between the four investigated cases (192 nm to 167 nm). Therefore, it is preferable to consider any *hp* profile rather than assuming *nhp* when considering lung deposition. The hygroscopicity significantly influences the deposition function (Fig 4b). For the total lung surface area (*TLSA*), the deposition minimum is found at 461 nm and 192 nm for the *nhp* and *hp*, respectively. In addition, the diameter of the minimum shifts significantly for the bronchi (*TB*) and deep lung (*AL*) (503 nm to 179 nm and 602 nm to 223 nm, respectively).

The shift is minimal for the upper airways (*EX*) from 259 nm to 223

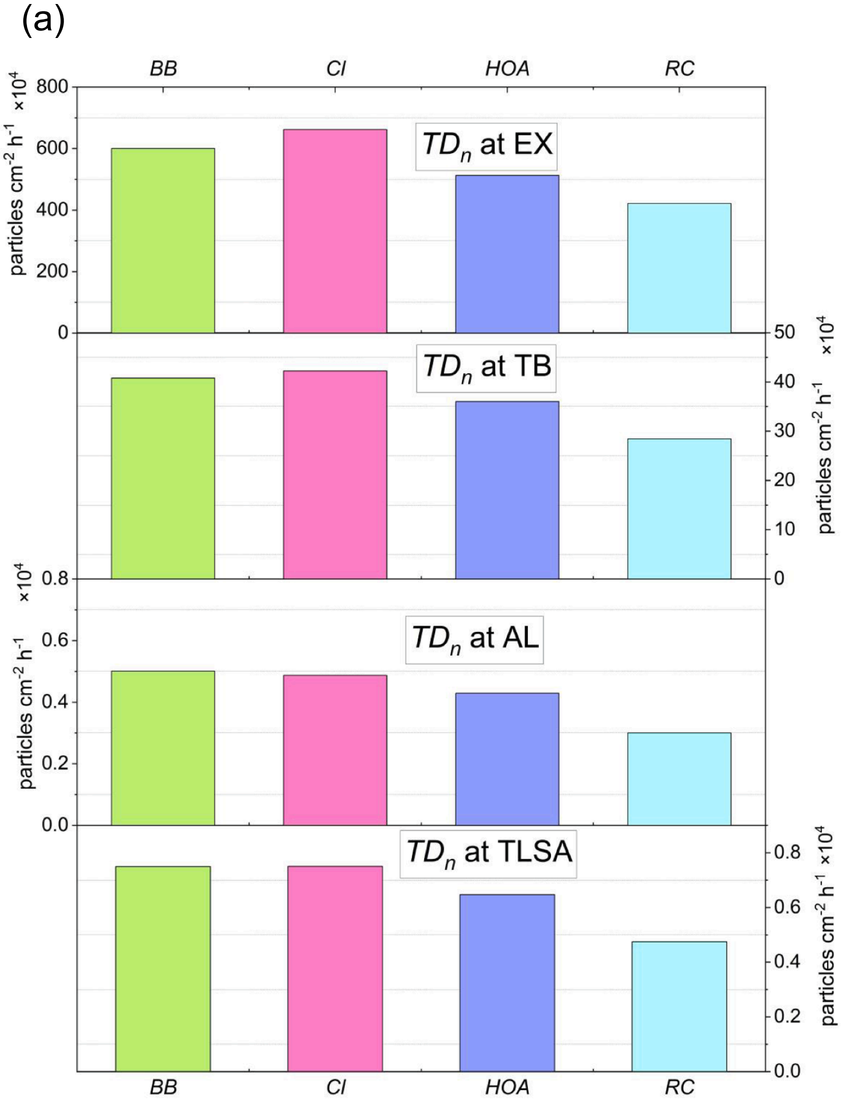

Fig. 5. Comparison of regional TD: a) deposited particle number (TD_n) and b) particle mass (TD_m) in the lung regions EX, TB, AL and TLSA during all investigative cases. The TLSA closely resembles the alveolar surface area (Section 2.8). There are notable differences in TD between the lung regions (see ordinates): The ratios EX: TLSA, TB: TLSA and AL: TLSA are 900, 60 and 0.6 for TD_n, respectively, and 700, 40 and 0.7 for TD_m, respectively, for the RC case.

nm, as *EX* is where particle growth begins. The “hygroscopic shift” of the deposition minimum has a two-way effect: For ultrafine and nanoparticles in the “thermodynamic regime”, the hygroscopic evolution lowers the *DE* compared to the *nhp*. For the fine particles in the “aerodynamic regime”, it increases the *DE*. There is a simultaneous decrease in deposited particle number and an increase in deposited particle mass when the mode in particle number (C_n) is typically below this deposition minimum and when the mode in particle mass (C_m) is beyond it (Table 3).

3.5. Impact of particle properties on tissue deposited number and mass

The airborne size distribution and the *DE* function are superimposed when calculating tissue deposition (*TD*). *TD* is, therefore, a new quality parameter. It differs from laboratory-based exposure and deposition experiments in that toxicologists usually use the number or mass of particles delivered to cells as a correlation parameter. Instead of assuming 100 % deposition for all particles of any diameter, *TD* also incorporates a fair prediction of the breathing pattern and deposition process. The factors TD_f (equations 4 and 5) contain all the density, hygroscopicity and deposition information. For similar pollution scenarios, they allow the *TD* to be calculated directly from the measured airborne data without explicitly running the HPLD model. The TD_f for the four investigative cases are provided in the supplementary file. The total tissue-deposited particle mass and number in the three lung regions and the total lung surface area are shown in Fig. 5. The lung region with the lowest surface area (*EX*) shows the most significant tissue deposition, indicating an inverse relationship between *TD* and the region’s total internal surface area. It has about 900 times more deposited particles than the mean (TLSA); the TB region has about 60 times more, and the *AL* region has about 2/3 more (see ordinates in Fig. 5a). Tissue deposited mass shows similar relationships (see ordinates in Fig. 5b). Table 3 shows the total TD_n and TD_m. The industrial emission case has the highest *TD*. The *Cl* and *RC* cases differ by about a factor of two (see column “Case: *RC*” in Table 3). Fig. 5b shows the highest deposited mass TD_m for the *Cl* case on total inner lung surface area, i.e. 28 pg cm^{-2}h^{-1}, followed by *BB* (22 pg cm^{-2}h^{-1}), *HOA* (17 pg cm^{-2}h^{-1}), and *RC* (14 pg cm^{-2}h^{-1})), as a high chloride content results in high hygroscopicity for 150 and 200 nm particles.

hp has a significantly lower deposited number (TD_n) than *nhp* (15 %

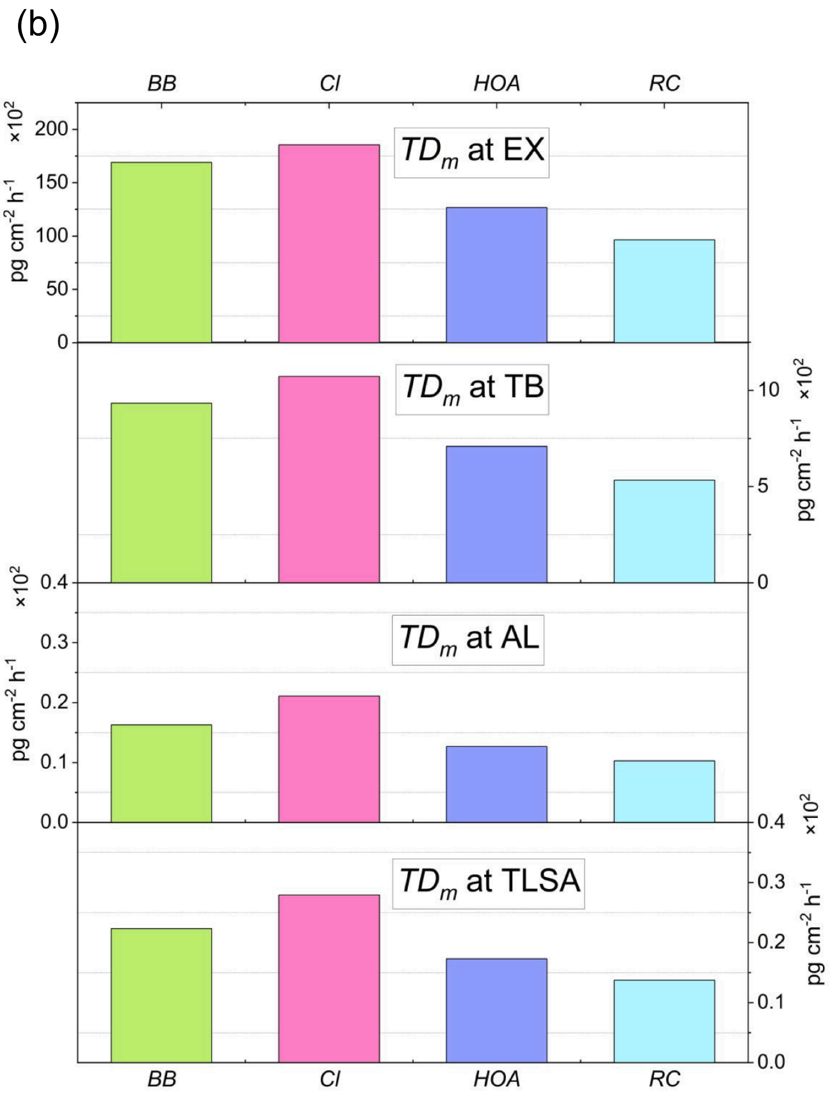

Fig. 5. (*continued*).

to 22 %; see Table 3 column $TD_n(hp)$: TD_n (ρ_0)). There is significantly overestimation of TD_n when all particles are assumed to be non-hygroscopic and of unit density.

The assumption that all particles are non-hygroscopic and of unit density again results in a significant underestimation of TD_m. It should be noted that the size, location, and deposition of a particle are altered by the water it absorbs as it passes through the respiratory system. Water uptake does not directly affect chemical loading or particle composition. After contact, the condensed water dissolves in the epithelial lining fluid, while the chemical load affects the cells.

Fig 4b illustrates the cause of the lower TD_n and higher TD_m for hygroscopic particles. The deposition minimum is “shifted” to smaller particle sizes by hygroscopicity. When $Dp < 200$ nm (quasi ultrafine size range), the deposition for *hp* is less than that for *nhp*. As the number distribution peaks at about 80 nm (see Fig. 1), the hygroscopic TD_n is reduced compared to the non-hygroscopic one. On the other hand, in the fine particle size range (~400 nm; see Fig. 2), the mass distribution peaks. The hygroscopic TD_m is, therefore, higher than the non-hygroscopic one. Overall, TD_n is reduced, and TD_m is simultaneously increased by the hygroscopic “minimum shift”.

3.6. Variations in diurnal tissue deposited number and mass

Fig. 6 and Tables 2 and 3 show the daytime and nighttime total deposition (*TD*) for each case studied. In contrast to the *RC* scenario, there is a consistently high deposition during both day and night for other episodes. The variation in the number of particles deposited for other episodes between day and night ranges from 2 % to 7 %. However, during the *RC* periods, the nighttime particle number deposition (TD_n) is reduced by 34 %.

The situation is even more pronounced for tissue mass deposition: TD_m is 23 % higher at night in the *HOA* case as compared to the daytime due to increased emissions from nighttime heavy duty diesel trucks. In other cases, such as *BB* and *Cl* (as shown in Fig. 6B and Table 3), higher daytime tissue mass deposition was observed i.e. 25 and 32 pg cm^{-2}h^{-1} respectively. In the case of *RC*, this nighttime tissue mass deposition reduction is almost three times greater than the daytime. Daytime tissue deposition was found to be high possibly due to highly hygroscopic particles during the RC case, although the number concentration of aerosol particles was significantly lower than other cases.

A notable discrepancy in *TD* is observed between the hygroscopic (*hp*) and non-hygroscopic (*nhp*) modelling cases. Fig. 6A shows a decrease in TD_n for the hygroscopic model (ranging from 0.78 to 0.85, as shown in Table 3), while Fig. 6B shows an increase in mass TD_m (ranging

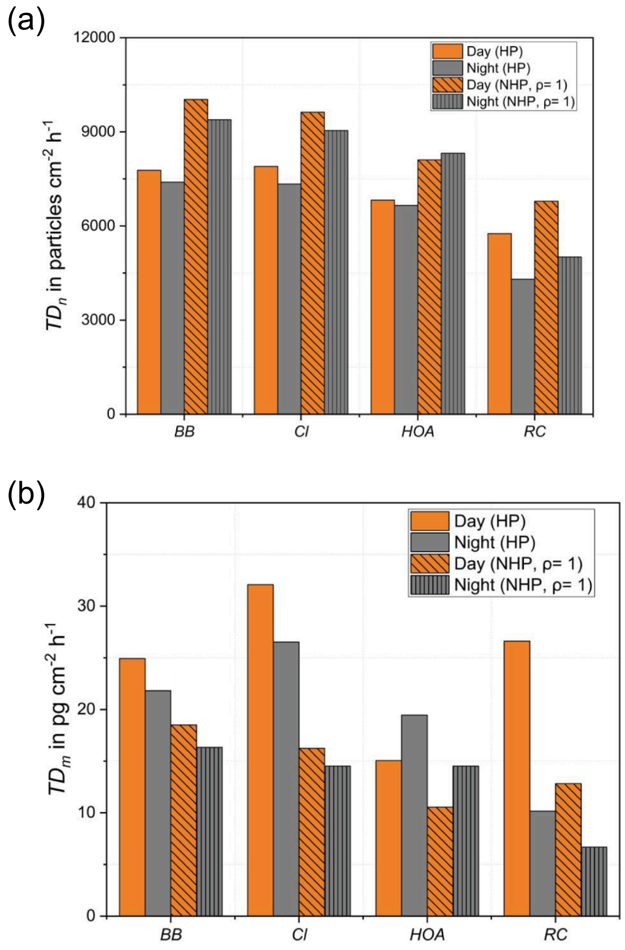

Fig. 6. Comparison of day and nighttime tissue deposition in the total lung. A) Tissue-deposited particle number- (TD_n) and B) tissue-deposited particle mass (TD_m), modelled for the total lung surface area (TLSA) surface area during the investigative cases biomass-burning (BB), chloride (Cl), vehicular emission (HOA), and relatively clean periods (RC). The ratio of day- vs. nighttime is listed in Table 3. TD is added with checked patterns for non-hygroscopic particles with density $\rho_0 = 1$ g cm^{-3}.

from 1.78 to 2.80, as shown in Table 3). This "hygroscopic shift" effect explains the observed increase in deposited mass and decrease in deposited particle number (see Section 3.5).

4. Conclusions

We modelled lung deposition for both hygroscopic and non-hygroscopic particles in four investigative cases – biomass burning, chloride (industrial emissions and waste burning), HOA (vehicle emissions) and relatively clean periods – using the measured hygroscopic growth factors (*GF*) in the Hygroscopic Particle Lung Deposition (HPLD) model. For non-hygroscopic particles, deposition typically reaches a minimum at around 450 nm. However, deposition modelling of hygroscopic particles shows that this minimum shifts to below 200 nm due to particle growth during respiratory transport. This shift increases the deposition of fine hygroscopic particles (>~400 nm) and reduces the deposition of particles below 200 nm. As the modal diameter of particle number distributions often falls below this "hygroscopic minimum", the total number of deposited particles is lower than non-hygroscopic particles. Conversely, when the modal diameter of the mass distribution is above this threshold, the deposited mass increases. Our model indicates a significant increase in particle mass deposition (1.8- to 2.8-fold) when particle density and hygroscopicity are considered. Comparative analysis of the different scenarios shows considerable variation in lung deposition rates. High chloride concentrations, characteristic of industrial and waste burning activities, are associated with the highest mass deposition to lung tissue, up to 28 pg cm^{-2}h^{-1}. Comparison of daytime and nighttime data shows consistently high particle loads during both time periods, with daytime concentrations exceeding nighttime concentrations by 6 % to 13 %. In particular, vehicle emissions show up to 23 % greater mass deposition on lung tissue at night, while chloride episodes show approximately 21 % greater mass deposition on lung tissue during the day, particularly in the early morning hours. This research highlights critical policy implications for mitigating the health risks associated with air pollution in Delhi, India. First, the results highlight the need to incorporate particle characteristics such as effective density and hygroscopicity into lung deposition models to assess lung deposition accurately. The regulatory efforts should prioritize measures to reduce emissions from biomass burning and vehicular emission sources (Liu et al., 2015; Romshoo et al., 2022) and thus potentially reduce lung deposition of harmful ultrafine particles. In addition, strategies to reduce industrial emissions and trash burning with high chloride contribution are imperative (Gani et al., 2019; Gunthe et al., 2021) as they were associated with increased hygroscopic growth and, consequently, higher tissue deposition rates. According to Glojek et al. (2024), Slovenia's cement sector has the highest oxidative potential (a measure for evaluating exposure) per µg of source for chloride concentrations. This suggests the toxic nature of chloride aerosol present in the atmosphere. Furthermore, our research emphasizes the significance of day-night differences in deposition patterns, pointing to the necessity of prompt actions customized for emission sources. These findings are ground-breaking for atmospheric science and have profound implications for public health and toxicology. Our research facilitates more accurate risk assessment and intervention strategies by providing novel parameters for interpreting exposure situations from a toxicological perspective.

CRediT authorship contribution statement

Anusmita Das: Writing – review & editing, Writing – original draft, Software, Data curation. **Erwin W. Karg:** Writing – review & editing, Writing – original draft, Validation, Software, Formal analysis, Data curation, Conceptualization. **George A. Ferron:** Writing – review & editing, Writing – original draft, Validation, Software, Formal analysis, Data curation, Conceptualization. **Jürgen Schnelle-Kreis:** Writing – review & editing, Writing – original draft. **Anil Kumar Mandariya:** Writing – review & editing, Writing – original draft, Visualization, Investigation, Data curation. **Gazala Habib:** Resources. **Alfred Wiedensohler:** Writing – review & editing, Resources. **Mira L. Pöhlker:** Writing – review & editing, Resources. **Ralf Zimmermann:** Writing – review & editing. **Ajit Ahlawat:** Writing – review & editing, Writing – original draft, Visualization, Investigation, Data curation, Conceptualization.

Declaration of competing interest

The authors declare that they have no known competing financial interests or personal relationships that could have appeared to influence the work reported in this paper.

Acknowledgements

We acknowledge Mohammed Haneef's support during the measurement campaign and Martin Sklorz and Narges Rastak's scientific support during the initial phases of the modelling work. We would also like to thank Subha Raj for her support during the data analysis.

Appendix A. Supplementary data

Supplementary data to this article can be found online at https://doi.org/10.1016/j.envint.2025.109548.

Data availability

Data will be made available on request.

References

Asgharian, B., Hofmann, W., Bergmann, R., 2001. Particle Deposition in a Multiple-Path Model of the Human Lung. Aerosol Sci. Technol. 34, 332–339. https://doi.org/10.1080/02786820119122.

Atkinson, D.B., Radney, J.G., Lum, J., Kolesar, K.R., Cziczo, D.J., Pekour, M.S., Zhang, Q., Setyan, A., Zelenyuk, A., Cappa, C.D., 2015. Aerosol optical hygroscopicity measurements during the 2010 CARES campaign. Atmospheric Chem. Phys. 15, 4045–4061. https://doi.org/10.5194/acp-15-4045-2015.

Brock, C.A., Wagner, N.L., Anderson, B.E., Attwood, A.R., Beyersdorf, A., Campuzano-Jost, P., Carlton, A.G., Day, D.A., Diskin, G.S., Gordon, T.D., Jimenez, J.L., Lack, D. A., Liao, J., Markovic, M.Z., Middlebrook, A.M., Ng, N.L., Perring, A.E., Richardson, M.S., Schwarz, J.P., Washenfelder, R.A., Welti, A., Xu, L., Ziemba, L.D., Murphy, D.M., 2016. Aerosol optical properties in the southeastern United States in summer – Part 1: Hygroscopic growth. Atmospheric Chem. Phys. 16, 4987–5007. https://doi.org/10.5194/acp-16-4987-2016.

Chee, S., Myllys, N., Barsanti, K.C., Wong, B.M., Smith, J.N., 2019. An Experimental and Modeling Study of Nanoparticle Formation and Growth from Dimethylamine and Nitric Acid. J. Phys. Chem. A 123, 5640–5648. https://doi.org/10.1021/acs.jpca.9b03326.

Chen, H., Chee, S., Lawler, M.J., Barsanti, K.C., Wong, B.M., Smith, J.N., 2018. Size resolved chemical composition of nanoparticles from reactions of sulfuric acid with ammonia and dimethylamine. Aerosol Sci. Technol. 52, 1120–1133. https://doi.org/10.1080/02786826.2018.1490005.

Ching, J., Kajino, M., 2018. Aerosol mixing state matters for particles deposition in human respiratory system. Sci. Rep. 8, 8864. https://doi.org/10.1038/s41598-018-27156-z.

Darquenne, C., Fleming, J.S., Katz, I., Martin, A.R., Schroeter, J., Usmani, O.S., Venegas, J., Schmid, O., 2016. Bridging the Gap Between Science and Clinical Efficacy: Physiology, Imaging, and Modeling of Aerosols in the Lung. J. Aerosol Med. Pulm. Drug Deliv. 29, 107–126. https://doi.org/10.1089/jamp.2015.1270.

Davidson, N., Tong, H.-J., Kalberer, M., Seville, P.C., Ward, A.D., Kuimova, M.K., Pope, F.D., 2017. Measurement of the Raman spectra and hygroscopicity of four pharmaceutical aerosols as they travel from pressurised metered dose inhalers (pMDI) to a model lung. Int. J. Pharm. 520, 59–69. https://doi.org/10.1016/j.ijpharm.2017.01.051.

Farkas, Á., Lizal, F., Jedelsky, J., Elcner, J., Karas, J., Belka, M., Misik, O., Jicha, M., 2020. The role of the combined use of experimental and computational methods in revealing the differences between the micron-size particle deposition patterns in healthy and asthmatic subjects. J. Aerosol Sci. 147, 105582. https://doi.org/10.1016/j.jaerosci.2020.105582.

Ferron, G.A., Haider, B., Kreyling, W.G., 1988a. Inhalation of salt aerosol particles—i. Estimation of the temperature and relative humidity of the air in the human upper airways. J. Aerosol Sci. 19, 343–363. https://doi.org/10.1016/0021-8502(88)90274-1.

Ferron, G.A., Kreyling, W.G., Haider, B., 1988b. Inhalation of salt aerosol particles—II. growth and deposition in the human respiratory tract. J. Aerosol Sci. 19, 611–631. https://doi.org/10.1016/0021-8502(88)90213-3.

Ferron, G.A., Upadhyay, S., Zimmermann, R., Karg, E., 2013. Model of the Deposition of Aerosol Particles in the Respiratory Tract of the Rat. II. Hygroscopic Particle Deposition. J. Aerosol Med. Pulm. Drug Deliv. 26, 101–119. https://doi.org/10.1089/jamp.2011.0965.

Gani, S., Bhandari, S., Seraj, S., Wang, D.S., Patel, K., Soni, P., Arub, Z., Habib, G., Hildebrandt Ruiz, L., Apte, J.S., 2019. Submicron aerosol composition in the world's most polluted megacity: the Delhi Aerosol Supersite study. Atmospheric Chem. Phys. 19, 6843–6859. https://doi.org/10.5194/acp-19-6843-2019.

Glojek, K., Dinh Ngoc Thuy, V., Weber, S., Uzu, G., Manousakas, M., Elazzouzi, R., Džepina, K., Darfeuil, S., Ginot, P., Jaffrezo, J.L., Žabkar, R., Turšič, J., Podkoritnik, A., Močnik, G., 2024. Annual variation of source contributions to PM10 and oxidative potential in a mountainous area with traffic, biomass burning, cement-plant and biogenic influences. Environ. Int. 189, 108787. https://doi.org/10.1016/j.envint.2024.108787.

Gunthe, S.S., Liu, P., Panda, U., Raj, S.S., Sharma, A., Darbyshire, E., Reyes-Villegas, E., Allan, J., Chen, Y., Wang, X., Song, S., Pöhlker, M.L., Shi, L., Wang, Y., Kommula, S. M., Liu, T., Ravikrishna, R., McFiggans, G., Mickley, L.J., Martin, S.T., Pöschl, U., Andreae, M.O., Coe, H., 2021. Enhanced aerosol particle growth sustained by high continental chlorine emission in India. Nat. Geosci. 14, 77–84. https://doi.org/10.1038/s41561-020-00677-x.

Haddrell, A.E., Davies, J.F., Miles, R.E.H., Reid, J.P., Dailey, L.A., Murnane, D., 2014. Dynamics of aerosol size during inhalation: Hygroscopic growth of commercial nebulizer formulations. Int. J. Pharm. 463, 50–61. https://doi.org/10.1016/j.ijpharm.2013.12.048.

Haddrell, A.E., Davies, J.F., Reid, J.P., 2015. Dynamics of Particle Size on Inhalation of Environmental Aerosol and Impact on Deposition Fraction. Environ. Sci. Technol. 49, 14512–14521. https://doi.org/10.1021/acs.est.5b01930.

Hitzenberger, R., Berner, A., Dusek, U., Alabashi, R., 1997. Humidity-Dependent Growth of Size-Segregated Aerosol Samples. Aerosol Sci. Technol. 27, 116–130. https://doi.org/10.1080/02786829708965461.

Hu, M., Peng, J., Sun, K., Yue, D., Guo, S., Wiedensohler, A., Wu, Z., 2012. Estimation of Size-Resolved Ambient Particle Density Based on the Measurement of Aerosol Number, Mass, and Chemical Size Distributions in the Winter in Beijing. Environ. Sci. Technol. 46, 9941–9947. https://doi.org/10.1021/es204073t.

Hussein, T., Löndahl, J., Paasonen, P., Koivisto, A.J., Petäjä, T., Hämeri, K., Kulmala, M., 2013. Modeling regional deposited dose of submicron aerosol particles. Sci. Total Environ. 458–460, 140–149. https://doi.org/10.1016/j.scitotenv.2013.04.022.

ICRP 66 recommendations (1994), n.d.

Karg, E.W., Ferron, G.A., Bauer, S., Di Bucchianico, S., Zimmermann, R., 2020. Is the particle deposition in a cell exposure facility comparable to the lungs? A computer model approach. Aerosol Sci. Technol. 54, 668–684. https://doi.org/10.1080/02786826.2020.1724868.

Kaviani, S., Piyanzina, I.I., Nedopekin, O.V., Tayurskii, D.A., 2022a. Adsorption behavior and sensing properties of toxic gas molecules onto PtnBe (n = 5, 7, 10) clusters: A DFT benchmark study. Mater. Today Commun. 33, 104851. https://doi.org/10.1016/j.mtcomm.2022.104851.

Kaviani, S., Shahab, S., Sheikhi, M., Ahmadianarog, M., 2019. DFT study on the selective complexation of meso-2,3-dimercaptosuccinic acid with toxic metal ions (Cd2+, Hg2+ and Pb2+) for pharmaceutical and biological applications. J. Mol. Struct. 1176, 901–907. https://doi.org/10.1016/j.molstruc.2018.09.027.

Kaviani, S., Tayurskii, D.A., Nedopekin, O.V., Piyanzina, I., 2022b. DFT insight into Cd2+, Hg2+, Pb2+, Sn2+, As3+, Sb3+, and Cr3+ heavy metal ions adsorption onto surface of bowl-like B30 nanosheet. J. Mol. Liq. 365, 120131. https://doi.org/10.1016/j.molliq.2022.120131.

Kristensson, A., Rissler, J., Löndahl, J., Johansson, C., Swietlicki, E., 2013. Size-Resolved Respiratory Tract Deposition of Sub-Micrometer Aerosol Particles in a Residential Area with Wintertime Wood Combustion. Aerosol Air Qual. Res. 13, 24–35. https://doi.org/10.4209/aaqr.2012.07.0194.

Laakso, L., Koponen, I.K., Mönkkönen, P., Kulmala, M., Kerminen, V.-M., Wehner, B., Wiedensohler, A., Wu, Z., Hu, M., 2006. Aerosol particles in the developing world; a comparison between New Delhi in India and Beijing in China. Water. Air. Soil Pollut. 173, 5–20. https://doi.org/10.1007/s11270-005-9018-5.

Lalchandani, V., Srivastava, D., Dave, J., Mishra, S., Tripathi, N., Shukla, A.K., Sahu, R., Thamban, N.M., Gaddamidi, S., Dixit, K., Ganguly, D., Tiwari, S., Srivastava, A.K., Sahu, L., Rastogi, N., Gargava, P., Tripathi, S.N., 2022. Effect of Biomass Burning on PM2.5 Composition and Secondary Aerosol Formation During Post-Monsoon and Winter Haze Episodes in Delhi. J. Geophys. Res. Atmospheres 127, e2021JD035232. https://doi.org/10.1029/2021JD035232.

Langridge, J.M., Richardson, M.S., Lack, D., Law, D., Murphy, D.M., 2011. Aircraft Instrument for Comprehensive Characterization of Aerosol Optical Properties, Part I: Wavelength-Dependent Optical Extinction and Its Relative Humidity Dependence Measured Using Cavity Ringdown Spectroscopy. Aerosol Sci. Technol. 45, 1305–1318. https://doi.org/10.1080/02786826.2011.592745.

Liu, Z., Hu, B., Ji, D., Wang, Y., Wang, M., Wang, Y., 2015. Diurnal and seasonal variation of the PM2.5 apparent particle density in Beijing. China. Atmos. Environ. 120, 328–338. https://doi.org/10.1016/j.atmosenv.2015.09.005.

Lizonova, D., Nagarkar, A., Demokritou, P., Kelesidis, G.A., 2024. Effective density of inhaled environmental and engineered nanoparticles and its impact on the lung deposition and dosimetry. Part. Fibre Toxicol. 21, 7. https://doi.org/10.1186/s12989-024-00567-9.

Man, R., Wu, Z., Zong, T., Voliotis, A., Qiu, Y., Größ, J., van Pinxteren, D., Zeng, L., Herrmann, H., Wiedensohler, A., Hu, M., 2022. Impact of water uptake and mixing state on submicron particle deposition in the human respiratory tract (HRT) based on explicit hygroscopicity measurements at HRT-like conditions. Atmospheric Chem. Phys. 22, 12387–12399. https://doi.org/10.5194/acp-22-12387-2022.

Mandariya, A.K., Ahlawat, A., Haneef, M., Baig, N.A., Patel, K., Apte, J., Hildebrandt Ruiz, L., Wiedensohler, A., Habib, G., 2024. Measurement report: Hygroscopicity of size-selected aerosol particles in the heavily polluted urban atmosphere of Delhi: impacts of chloride aerosol. Atmospheric Chem. Phys. 24, 3627–3647. https://doi.org/10.5194/acp-24-3627-2024.

Mandariya, A.K., Tripathi, S.N., Gupta, T., Mishra, G., 2020. Wintertime hygroscopic growth factors (HGFs) of accumulation mode particles and their linkage to chemical composition in a heavily polluted urban atmosphere of Kanpur at the Centre of IGP, India: Impact of ambient relative humidity. Sci. Total Environ. 704, 135363. https://doi.org/10.1016/j.scitotenv.2019.135363.

Massling, A., Leinert, S., Wiedensohler, A., Covert, D., 2007. Hygroscopic growth of sub-micrometer and one-micrometer aerosol particles measured during ACE-Asia. Atmospheric Chem. Phys. 7, 3249–3259. https://doi.org/10.5194/acp-7-3249-2007.

McMurry, P.H., Stolzenburg, M.R., 1989. On the sensitivity of particle size to relative humidity for Los Angeles aerosols. Atmospheric Environ. 1967 (23), 497–507. https://doi.org/10.1016/0004-6981(89)90593-3.

Morawska, L., Buonanno, G., 2021. The physics of particle formation and deposition during breathing. Nat. Rev. Phys. 3, 300–301. https://doi.org/10.1038/s42254-021-00307-4.

Oberdörster, G., 2000. Pulmonary effects of inhaled ultrafine particles. Int. Arch. Occup. Environ. Health 74, 1–8. https://doi.org/10.1007/s004200000185.

Peppas, N.A., 1984. Wissenschaftliche tabellen Geigy (Scientific tables Geigy): four volumes, Ciba-Geigy A.G., Basle, Switzerland, 1980, 1144 pages, S.Fr. 15 per volume. J. Controlled Release 1, 83.

Perwitzschky, R., 1928. Die Temperatur und Feuchtigkeitsverhältnisse der Atemluft in den Luftwegen. Arch. Für Ohren- Nasen- Kehlkopfheilkd. 117, 1–36.

Petters, M.D., Kreidenweis, S.M., 2007. A single parameter representation of hygroscopic growth and cloud condensation nucleus activity. Atmospheric Chem. Phys. 7, 1961–1971. https://doi.org/10.5194/acp-7-1961-2007.

Rissler, J., Vestin, A., Swietlicki, E., Fisch, G., Zhou, J., Artaxo, P., Andreae, M.O., 2006. Size distribution and hygroscopic properties of aerosol particles from dry-season biomass burning in Amazonia. Atmos Chem Phys 6, 471–491. https://doi.org/10.5194/acp-6-471-2006.

Romshoo, B., Müller, T., Ahlawat, A., Wiedensohler, A., Haneef, M.V., Imran, M., Warsi, A.B., Mandariya, A.K., Habib, G., Pöhlker, M.L., 2024. Significant contribution of fractal morphology to aerosol light absorption in polluted environments dominated by black carbon (BC). Npj Clim. Atmospheric Sci. 7, 87. https://doi.org/10.1038/s41612-024-00634-0.

Romshoo, B., Pöhlker, M., Wiedensohler, A., Pfeifer, S., Saturno, J., Nowak, A., Ciupek, K., Quincey, P., Vasilatou, K., Ess, M.N., Gini, M., Eleftheriadis, K., Robins, C., Gaie-Levrel, F., Müller, T., 2022. Importance of size representation and morphology in modelling optical properties of black carbon: comparison between laboratory measurements and model simulations. Atmospheric Meas. Tech. 15, 6965–6989. https://doi.org/10.5194/amt-15-6965-2022.

Sarangi, B., Aggarwal, S.G., Sinha, D., Gupta, P.K., 2016. Aerosol effective density measurement using scanning mobility particle sizer and quartz crystal microbalance with the estimation of involved uncertainty. Atmospheric Meas. Tech. 9, 859–875. https://doi.org/10.5194/amt-9-859-2016.

Schmid, O., Bolle, I., Harder, V., Karg, E., Takenaka, S., Schulz, H., Ferron, G.A., 2008. Model for the Deposition of Aerosol Particles in the Respiratory Tract of the Rat. I. Nonhygroscopic Particle Deposition. J. Aerosol Med. Pulm. Drug Deliv. 21, 291–308. https://doi.org/10.1089/jamp.2008.0689.

Schmid, O., Karg, E., Hagen, D.E., Whitefield, P.D., Ferron, G.A., 2007. On the effective density of non-spherical particles as derived from combined measurements of aerodynamic and mobility equivalent size. J. Aerosol Sci. 38, 431–443. https://doi.org/10.1016/j.jaerosci.2007.01.002.

Speer, R.E., Barnes, H.M., Brown, R., 1997. An Instrument for Measuring the Liquid Water Content of Aerosols. Aerosol Sci. Technol. 27, 50–61. https://doi.org/10.1080/02786829708965457.

Swietlicki, E., Hansson, H.-C., Hämeri, K., Svenningsson, B., Massling, A., McFiggans, G., McMurry, P.H., Petäjä, T., Tunved, P., Gysel, M., Topping, D., Weingartner, E., Baltensperger, U., Rissler, J., Wiedensohler, A., Kulmala, M., 2008. Hygroscopic properties of submicrometer atmospheric aerosol particles measured with H-TDMA instruments in various environments—a review. Tellus B 60, 432–469. https://doi.org/10.1111/j.1600-0889.2008.00350.x.

Voliotis, A., Samara, C., 2018. Submicron particle number doses in the human respiratory tract: implications for urban traffic and background environments. Environ. Sci. Pollut. Res. 25, 33724–33735. https://doi.org/10.1007/s11356-018-3253-y.

Vu, T.V., Zauli-Sajani, S., Poluzzi, V., Harrison, R.M., 2018. Factors controlling the lung dose of road traffic-generated sub-micrometre aerosols from outdoor to indoor environments. Air Qual. Atmosphere Health 11, 615–625. https://doi.org/10.1007/s11869-018-0568-2.

Wang, X., Shen, X.J., Sun, J.Y., Zhang, X.Y., Wang, Y.Q., Zhang, Y.M., Wang, P., Xia, C., Qi, X.F., Zhong, J.T., 2018. Size-resolved hygroscopic behavior of atmospheric aerosols during heavy aerosol pollution episodes in Beijing in December 2016. Atmos. Environ. 194, 188–197. https://doi.org/10.1016/j.atmosenv.2018.09.041.

Wiedensohler, A., Birmili, W., Nowak, A., Sonntag, A., Weinhold, K., Merkel, M., Wehner, B., Tuch, T., Pfeifer, S., Fiebig, M., Fjäraa, A.M., Asmi, E., Sellegri, K., Depuy, R., Venzac, H., Villani, P., Laj, P., Aalto, P., Ogren, J.A., Swietlicki, E., Williams, P., Roldin, P., Quincey, P., Hüglin, C., Fierz-Schmidhauser, R., Gysel, M., Weingartner, E., Riccobono, F., Santos, S., Grüning, C., Faloon, K., Beddows, D., Harrison, R., Monahan, C., Jennings, S.G., O'Dowd, C.D., Marinoni, A., Horn, H.-G., Keck, L., Jiang, J., Scheckman, J., McMurry, P.H., Deng, Z., Zhao, C.S., Moerman, M., Henzing, B., de Leeuw, G., Löschau, G., Bastian, S., 2012. Mobility particle size spectrometers: harmonization of technical standards and data structure to facilitate high quality long-term observations of atmospheric particle number size distributions. Atmospheric Meas. Tech. 5, 657–685. https://doi.org/10.5194/amt-5-657-2012.

World Air Qual. Rep. 1–35, 2019, n.d.

Wu, Z.J., Poulain, L., Henning, S., Dieckmann, K., Birmili, W., Merkel, M., van Pinxteren, D., Spindler, G., Müller, K., Stratmann, F., Herrmann, H., Wiedensohler, A., 2013. Relating particle hygroscopicity and CCN activity to chemical composition during the HCCT-2010 field campaign. Atmospheric Chem. Phys. 13, 7983–7996. https://doi.org/10.5194/acp-13-7983-2013.

Yeh, H.-C., Schum, G.M., 1980. Models of human lung airways and their application to inhaled particle deposition. Bull. Math. Biol. 42, 461–480. https://doi.org/10.1016/S0092-8240(80)80060-7.

Zhang, S.L., Ma, N., Kecorius, S., Wang, P.C., Hu, M., Wang, Z.B., Größ, J., Wu, Z.J., Wiedensohler, A., 2016. Mixing state of atmospheric particles over the North China Plain. Atmos. Environ. 125, 152–164. https://doi.org/10.1016/j.atmosenv.2015.10.053.

Zhang, X., Massoli, P., Quinn, P.K., Bates, T.S., Cappa, C.D., 2014. Hygroscopic growth of submicron and supermicron aerosols in the marine boundary layer. J. Geophys. Res. Atmospheres 119, 8384–8399. https://doi.org/10.1002/2013JD021213.

Zhou, Y., Ma, N., Wang, Q., Wang, Z., Chen, C., Tao, J., Hong, J., Peng, L., He, Y., Xie, L., Zhu, S., Zhang, Y., Li, G., Xu, W., Cheng, P., Kuhn, U., Zhou, G., Fu, P., Zhang, Q., Su, H., Cheng, Y., 2022. Bimodal distribution of size-resolved particle effective density: results from a short campaign in a rural environment over the North China Plain. Atmospheric Chem. Phys. 22, 2029–2047. https://doi.org/10.5194/acp-22-2029-2022.

Zong, T., Wang, H., Wu, Z., Lu, K., Wang, Y., Zhu, Y., Shang, D., Fang, X., Huang, X., He, L., Ma, N., Größ, J., Huang, S., Guo, S., Zeng, L., Herrmann, H., Wiedensohler, A., Zhang, Y., Hu, M., 2022. Particle hygroscopicity inhomogeneity and its impact on reactive uptake. Sci. Total Environ. 811, 151364. https://doi.org/10.1016/j.scitotenv.2021.151364.